sustainability

MDPI

Article

Hydraulic and Structural Numerical Assessment of a Smart Rubber and Steel Movable Weir for Selective Gate Operation

Mi Sol Kim [1], Jae-Hyuk Koo [1], Derick Gabriel Stein [2], Su-Jin Lee [3], Chan-Gi Park [4,*] and Jaeheum Yeon [5,*]

[1] Department of Agricultural Engineering, Kongju National University, Yesan 32439, Republic of Korea; dkzkap5198@naver.com (M.S.K.); d20250151@smail.kongju.ac.kr (J.-H.K.)
[2] Interdisciplinary Program in Earth Environmental System Science & Engineering, Kangwon National University, Chuncheon 24341, Republic of Korea; gabriel.stein@kangwon.ac.kr
[3] Department of Architectural Engineering, Keimyung University, Daegu 42601, Republic of Korea; sjlee@kmu.ac.kr
[4] Department of Regional Construction Engineering, Kongju National University, Yesan 32439, Republic of Korea
[5] Department of Regional Infrastructure Engineering, Kangwon National University, Chuncheon 24341, Republic of Korea
* Correspondence: cgpark@kongju.ac.kr (C.-G.P.); jyeon@kangwon.ac.kr (J.Y.)

Abstract

Conventional full-span movable weirs may require complete lowering for sediment or debris release, reducing upstream water-level control and limiting operational efficiency. This study evaluates a smart rubber and steel (SRS) movable weir that enables selective gate operation through a one-way coupled hydraulic–structural framework using the Environmental Fluid Dynamics Code (EFDC) and MIDAS Civil. Four gate-operation scenarios and gate heights of 0.5, 1.0, 1.5, and 2.0 m were analyzed to characterize flow redistribution, hydraulic loading, gate response, longitudinal-rib performance, and the safety of anchor bolts, clamping plates, and the airbag system. Selective lowering substantially altered flow distribution, with side-gate lowering producing the most critical condition and increasing maximum velocity by approximately 267% relative to the fully raised condition at a 2.0 m gate height. Hydraulic demand became strongly localized near the lowered and adjacent raised spans, although the governing static load remained dominated by hydrostatic loading. Rib comparisons showed that redistributing stiffness through additional longitudinal stiffeners reduced stress and deformation without relying solely on gate thickening, while all component-level static checks satisfied the adopted safety criteria. The results demonstrate that integrating span-specific hydraulic redistribution with structural response provides a practical basis for structurally safe and material-efficient river-infrastructure design.

Keywords: steel and rubber weir; movable weir; river infrastructure; EFDC simulation; MIDAS Civil; material-efficient design

Check for updates

Academic Editor: Giuseppe Barbaro

Received: 24 July 2026
Revised: 21 August 2026
Accepted: 24 August 2026
Published: 25 August 2026

Copyright: © 2026 by the authors. Licensee MDPI, Basel, Switzerland. This article is an open access article distributed under the terms and conditions of the Creative Commons Attribution (CC BY) license.

1. Introduction

Weirs are in-river structures that provide power generation, flood control and a means of redirecting water resources for human consumption [1]. Low-head river barriers and conventional fixed weirs can provide these functions, but their impounding effect modifies local hydraulics and sediment continuity by reducing flow velocity and promoting upstream sediment deposition [2–4]. Fine-grained sediment accumulation is particularly important because it is associated with water-quality degradation, contaminant transport,

habitat alteration, and ecological stress in river systems [5–7]. In regulated rivers, interrupted sediment transport can also reduce the long-term functionality of water-control infrastructure by decreasing effective storage, altering channel morphology, and increasing the need for sediment-management operations [3,7]. Therefore, river-control structures require not only adequate hydraulic performance but also operational strategies that can release accumulated sediment while maintaining stable flow conditions and long-term operational functionality. The environmental significance of sediment regulation also extends beyond channel morphology and storage capacity. For example, large-scale water-sediment regulation in the Yellow River was reported to alter the composition and transformation characteristics of dissolved organic matter in the estuarine environment, indicating that engineered changes in water and sediment delivery can influence downstream aquatic chemistry [8]. Such findings further emphasize the need for hydraulic structures that can manage sediment release while maintaining stable water-control functionality.

Integrated movable weirs and inflatable rubber weirs can overcome some limitations of their fixed counterparts, but many systems still operate by lowering the entire span when sediment or floating debris must be discharged. This full-span operation can reduce upstream water level even when sediment is locally accumulated near only a portion of the weir. Additionally, suspended and bedload sediment transfer across weir-like structures is event-dependent and spatially variable, indicating that sediment-release performance should be evaluated together with local hydraulic behavior [9]. Smart rubber and steel (SRS) movable weirs provide selective discharge through individually controlled airbags supporting each gate span [10]. Technical development projects have established the basic configuration, selective-operation concept, and component design of hybrid rubber–steel movable weirs [11]. By varying the internal air pressure, individual spans can be lowered where floating debris or sediment has accumulated, thereby limiting the reduction in upstream water level associated with the complete lowering of conventional movable weirs. However, selective gate lowering may produce concentrated flow, asymmetric hydraulic loading, and localized structural demand that are not captured by water-level control alone. It has been emphasized that similar discharge or water-level conditions may generate different local flow patterns around hydraulic structures, which can influence scour, vibration, and operational safety [12]. The structural safety of the gate, longitudinal reinforcing ribs, anchor bolts, clamping plates, and airbags must therefore be evaluated under different selective-operation conditions.

Recent research relevant to selectively operated movable weirs can be categorized into hydraulic, structural, and advanced numerical-analysis approaches. From a hydraulic perspective, experimental investigation of a rising sector gate showed that gate-opening conditions substantially influence local velocity and turbulence characteristics [13]. Experimental and numerical analyses of a multi-plate vertical rotary gate further demonstrated that operating conditions can markedly alter local flow behavior [14]. Structural studies of movable-weir systems have meanwhile examined gate-panel behavior, reinforcement configurations, hybrid steel-composite components, clamping systems, and other load-carrying elements. More recently, advanced numerical methods have been developed for transient structural response under time-dependent and fluid-associated loading, including a numerically stable transient-analysis framework for thin-walled cylindrical shells [15] and transient vibration analysis of underwater cylindrical shells [16]. Although these studies advance the hydraulic or structural analysis of controlled hydraulic structures and fluid-loaded structural systems, hydraulic redistribution, gate response, and component-level safety are generally examined separately. Numerical investigations that directly connect selective operation of independently controlled hybrid rubber–steel gate spans with

three-dimensional span-specific hydraulic loading and subsequent structural assessment therefore remain limited.

In addition, the sustainability of river infrastructure depends not only on hydraulic function but also on material-efficient structural design, component reliability, maintenance demand, and service life. Stiffened plate studies have shown that stiffener layout can strongly influence stress distribution, buckling resistance, and structural weight, suggesting that rib configuration may provide a material-efficient alternative to plate thickening [17,18]. Previous life-cycle studies of dam infrastructure also indicate that maintenance, retrofitting, and end-of-life stages should be considered when evaluating long-term sustainability [19,20]. Within this context, the contribution of the present study to lower-carbon hydraulic infrastructure is positioned at the structural design-decision level. By comparing longitudinal-rib arrangements with plate thickening and verifying the safety of the principal load-transfer components, the proposed framework identifies opportunities to improve structural efficiency without relying solely on additional material. Maintaining adequate component capacity may also help reduce unnecessary material use and premature component replacement. Accordingly, the present assessment provides engineering inputs for subsequent life-cycle assessment and cost–carbon optimization of movable-weir alternatives, through which the environmental benefits of material-efficient configurations can be quantified more explicitly.

Previous studies of gated weirs and hydraulic-control structures have primarily examined discharge characteristics and local flow behavior under partial gate-opening conditions. However, these studies generally treat gate operation as a hydraulic problem, and comparatively little attention has been given to how the selective lowering of individual spans redistributes three-dimensional hydraulic loads between the lowered and adjacent gates and transfers those loads to structural components. Consequently, the structural implications of selective operation, including the influence of longitudinal-rib configuration and the safety of the anchor bolts, clamping plates, and airbag system, remain insufficiently established. This study addresses this gap by coupling Environmental Fluid Dynamics Code (EFDC) hydrodynamic simulations with component-level MIDAS Civil structural analysis. EFDC was originally developed at the Virginia Institute of Marine Science and is a multifunctional surface-water model capable of three-dimensional simulation of hydrodynamics and constituent transport [21,22]. The model has been applied to rivers, lakes, reservoirs, wetlands, estuaries, and coastal waters and includes functions for wetting and drying, sediment transport, and hydraulic-structure representation. Four selective gate-operation scenarios were evaluated to characterize scenario-specific flow distributions and hydraulic loads. The resulting loads were transferred to the structural model to assess gate response, compare longitudinal-rib configurations, and verify the safety of the principal load-carrying components. By coupling span-specific hydrodynamic loading with component-level structural assessment, this study clarifies how selective operation affects both hydraulic behavior and the safety of individual components within the SRS movable-weir system. Compared with experimental approaches and more advanced transient numerical formulations, the present EFDC-MIDAS framework involves several simplifications, including steady-state one-way hydraulic-to-structural load transfer, idealized structural boundary conditions, and the absence of explicit transient fluid–structure interaction. These limitations define the framework as a preliminary static assessment and may be addressed in future studies through grid-convergence analysis, transient two-way coupling, nonlinear contact modeling, and physical or field validation. Nevertheless, the adopted approach provides a practical basis for relating selective gate operation to span-specific hydraulic loading and component-level structural response under the analyzed conditions.

2. Methods

Figure 1 summarizes the coupled EFDC–MIDAS Civil framework adopted in this study. EFDC (EFDC+ version 12.5, DSI LLC, Edmonds, WA, USA) was used to simulate velocity and water-level distributions under four selective gate-operation scenarios. The resulting scenario-specific hydraulic loads were calculated and transferred to MIDAS Civil 2026 (MIDAS Information Technology Co., Ltd., Republic of Korea) to evaluate the structural responses of the gate body, longitudinal ribs, anchor bolts, clamping plates, and airbag system.

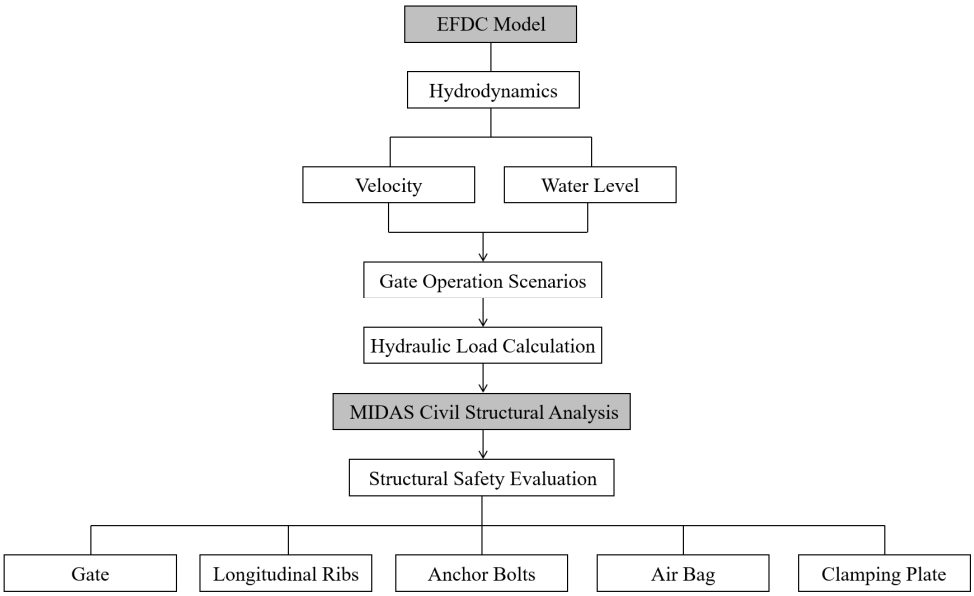


Figure 1. Coupled Environmental Fluid Dynamics Code (EFDC)–MIDAS Civil workflow for the hydraulic and component-level structural safety assessment of the smart rubber and steel (SRS) movable weir.

2.1. Model Parameters and Gate-Operation Scenarios

The gate-height cases and selective operating states were treated as separate parameters in the numerical analysis. Four nominal gate heights of 0.5, 1.0, 1.5, and 2.0 m were evaluated, while a standing angle of 50° was prescribed for the raised gate configuration. This angle defines the geometric orientation used in calculating the hydrostatic and self-weight components acting on a raised gate and was maintained consistently when comparing the four nominal gate-height cases. The 2.0 m case consequently represented the greatest hydraulic load among the evaluated heights and was subsequently used in the governing structural assessment, including the raised gate adjacent to the lowered span in the critical side-lowering scenario. Selective operation is achieved by controlling the pressure of the supporting airbags. In the present analysis, however, the raised and lowered gate configurations were prescribed for each operating scenario, and the gate motion during airbag inflation or deflation was not simulated. The material properties adopted for the SRS gate and its load-carrying components are summarized in Table 1.

The river conditions used in the hydraulic model were based on the Korean River Directory and flow-duration data from the Water Resources Information System (WAMIS). The model stream length was set to 150.0 m, consisting of 75.0 m upstream and 75.0 m downstream of the SRS gate, with a stream width of 25.0 m and a bed slope of 0.004. A flow rate of 0.146 m^3/s was applied under ordinary-flow and steady-state conditions. Because this discharge represents a flow-duration-based ordinary-flow condition rather than a frequency-based design event, a recurrence interval was not assigned. The adopted dis-

charge provides a common ordinary-flow condition for comparing the hydraulic response among the selective gate-operation scenarios. The computational domain was set to 25.0 m in the transverse direction and 150.0 m in the longitudinal direction. The grid size ranged from 0.25 m × 0.25 m near the SRS gate to 2.65 m × 6.225 m in the outer domain. A total of 5896 grid cells were used, including 600 cells assigned to the SRS gate region. Local refinement was concentrated around the SRS gate, where the minimum horizontal grid size corresponded to approximately 20 cells across each 5.0 m gate span. The same grid configuration was applied to all gate-operation scenarios to provide a consistent numerical basis for comparative evaluation of flow redistribution. However, a formal grid-convergence study using systematically refined meshes was not performed in the original numerical analysis. Accordingly, mesh independence of the absolute peak velocities and derived hydraulic forces cannot be established, and these quantities should be interpreted with respect to the adopted spatial resolution. The elevation range of the model was 4.75 m, from EL. 97.63 m to EL. 102.38 m, and a curvilinear orthogonal coordinate system was applied to represent the channel and gate region, as shown in Figure 2.

Table 1. Material properties of the SRS movable-weir components used.

Component	Material or Grade	Design Parameter	Value
Gate and longitudinal ribs	ASTM A572 Grade 50 steel	Reference strength	345 MPa
Anchor bolts	STS304 stainless steel	Bolt diameter	24 mm
		Cross-sectional area	353 mm^2
		Embedment depth	237 mm
		Installation spacing	200 mm
		No.	5
		Ultimate tensile strength	520 MPa (5300 kgf/cm^2)
Clamping plate	STS304 stainless steel	Width	180 mm
		Length	1000 mm
		Thickness	25 mm
		0.2% Proof strength	210 MPa
Airbag	Rubber airbag with reinforcing fabric	Reinforcing-fabric strength	180 kgf/cm^2 (17.65 MPa)
Concrete crest	Concrete	Compressive strength	23.5 MPa (240 kgf/cm^2)

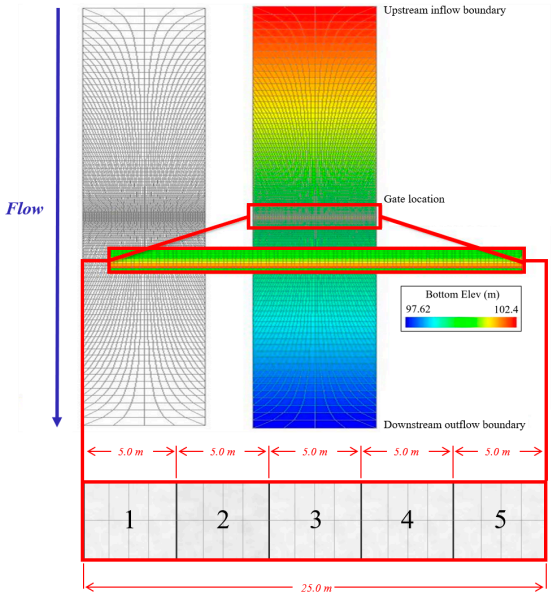
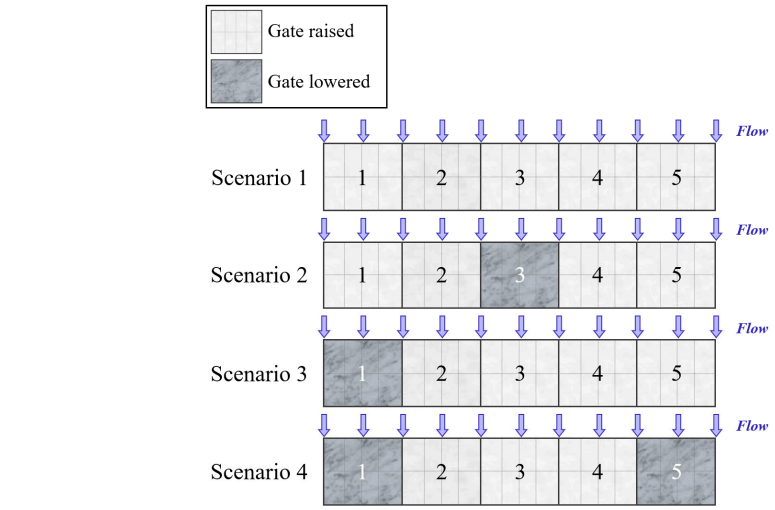
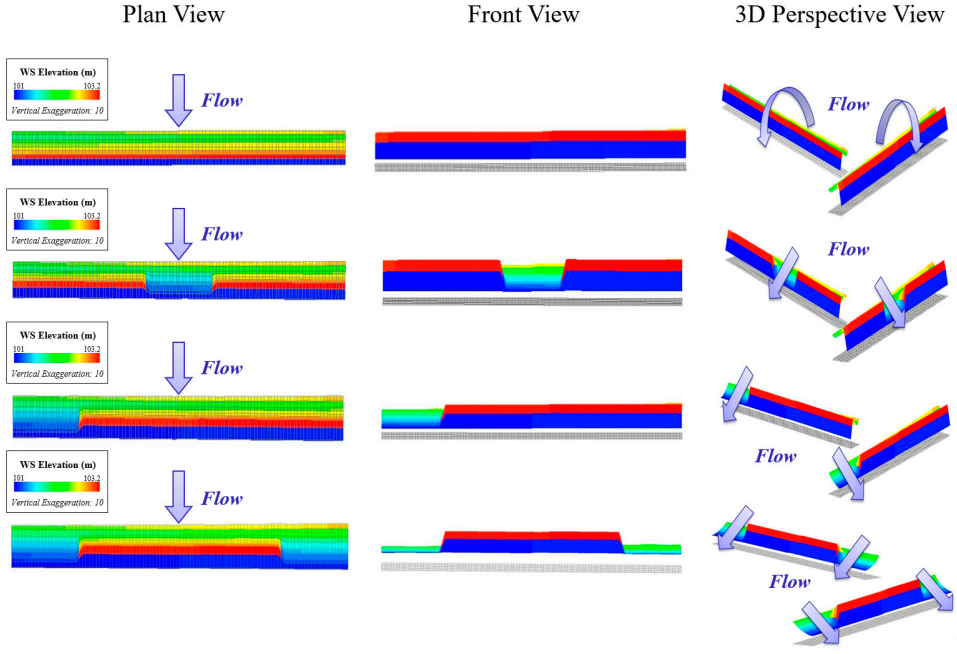


Figure 2. Plan view of the EFDC computational domain showing the grid configuration, bottom elevation, SRS gate location, and upstream downstream hydraulic boundaries, and gate numbers 1–5.

Four operating scenarios were defined to represent different selective-discharge conditions. Figure 3a provides a schematic representation of the raised and lowered gate positions, while Figure 3b shows the corresponding EFDC model configurations in plan, front, and 3D perspective views. Scenario 1 represents the fully raised condition, in which Gates 1–5 are raised. Scenario 2 represents central lowering, in which Gate 3 is lowered while Gates 1, 2, 4, and 5 remain raised. Scenario 3 represents side lowering, in which Gate 1 is lowered while Gates 2–5 remain raised. Scenario 4 represents dual-side lowering, in which Gates 1 and 5 are lowered while Gates 2–4 remain raised. These scenarios were selected to compare distributed overflow under the fully raised condition with concentrated discharge through selected lowered gate spans.



(**a**)



(**b**)

Figure 3. SRS gate-operation scenarios used in the EFDC model: (**a**) schematic representation of raised and lowered gate spans, with numbers 1–5 indicating the individual gates; (**b**) corresponding model configurations shown in plan view, front view, and 3D perspective view.

2.2. Hydraulic Loading and External-Force Derivation

Figure 4 illustrates the primary loads acting on the SRS gate: the hydrostatic pressure induced by impounded water and the horizontal component of the gate self-weight.

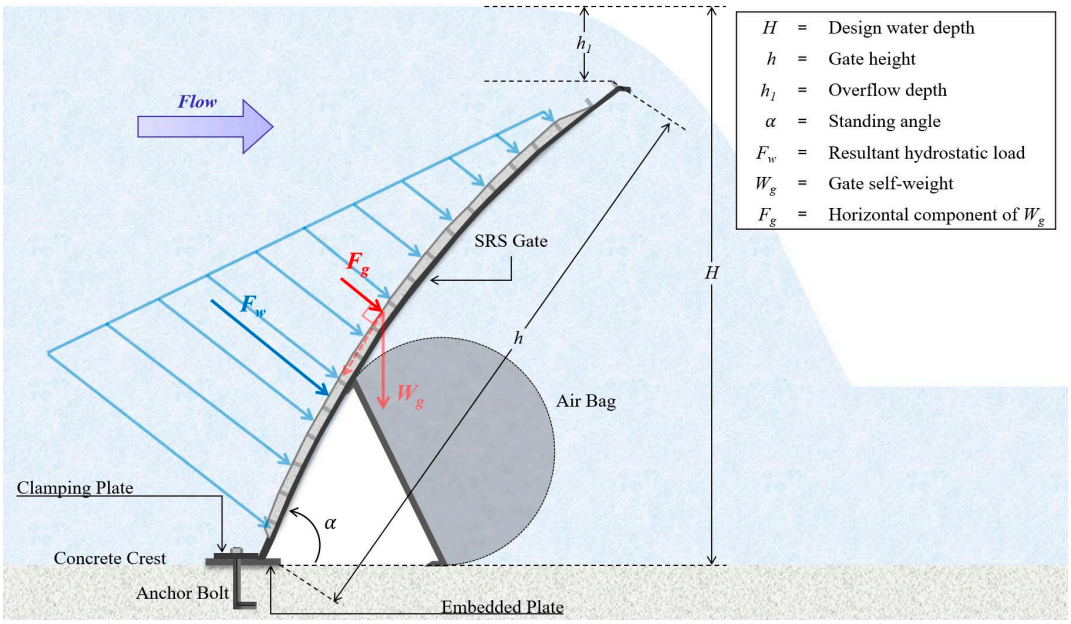


Figure 4. Hydraulic-load parameters acting on the SRS gate.

Because the SRS gate is installed at an inclined standing angle, the hydrostatic load acting normal to the gate surface was calculated using the conventional hydrostatic-force formulation for a submerged inclined surface [23]:

$$F_w = \frac{\gamma_0 B\left(H^2 - {h_1}^2\right)}{2sin\alpha} \quad (1)$$

where F_w is the hydraulic load acting on the gate (in kN), γ_0 is the unit weight of water (in kN/m^3), B is the gate width (in m), H is the design water depth (in m), h_1 is the overflow depth (in m), and α is the standing angle of the gate (in degrees). In this study, γ_0, B, h_1, and α were set to 9.8 kN/m^3, 5.0 m, 0.4 m, and 50°, respectively. The horizontal component of the gate self-weight was calculated using Equation (2):

$$F_g = W_g cos\alpha \quad (2)$$

where F_g is the horizontal component of the gate self-weight (in kN) and W_g is the gate weight (in kN). A gate weight of 3.43 kN (350 kg) was applied. The calculated load components for each gate-height case are summarized in Table 2.

Table 2. Loads applied to the SRS gate according to gate height.

Load Component	Gate Height			
	2.0 m	**1.5 m**	**1.0 m**	**0.5 m**
Hydraulic load, F_w (kN)	179.10	110.34	57.57	20.79
Horizontal component of W_g, F_g (kN)	2.20	2.20	2.20	2.20
Total load	181.31	112.54	59.77	22.99

The flow-induced external-force distribution was derived from the EFDC velocity field using the impulse–momentum relationship [23]. The simulated velocity vector was decomposed into the x-component parallel to the SRS gate and the y-component normal to the gate. Because the normal component directly contributes to the force acting on the gate surface, the y-component velocity was used to estimate the flow-induced external force as follows:

$$F_f = \rho Q(v_2 - v_1) \quad (3)$$

where F_f is the flow-induced external force (in N), ρ is the water density (in kg/m^3), Q is the discharge (in m^3/s), v_2 is the EFDC-derived velocity component used for the force calculation (in m/s), and v_1 is the initial velocity (in m/s). In this study, ρ was set to 1000 kg/m^3, and v_1 was set to 0 m/s to represent the stationary gate/projection wall used as the reference surface. The calculated cell-level external-force distribution was then converted into a conservative span-level force using the maximum cell force:

$$F_{f,span} = F_{cell,\,max} N_c \quad (4)$$

where $F_{\mathrm{cell,max}}$ is the maximum force obtained from the divided gate-span cells (in N), and N_c is the number of cells in one gate span. This procedure provided an equivalent span-level flow-induced load for the subsequent structural safety assessment.

The hydraulic-load formulation adopted in this study represents a steady-state loading condition. Hydrostatic loading, the gate self-weight component, and the momentum-based force derived from the EFDC velocity field were considered, whereas transient pressure fluctuations associated with vortex shedding, flow separation, downstream recirculation, and negative-pressure effects were not explicitly evaluated. Such effects contribute to dynamic loading of hydraulic gates under asymmetric gate-operation conditions [24,25] and should therefore be considered in future transient or fluid–structure interaction analyses.

2.3. Structural Modeling of the SRS Gate and Longitudinal-Rib Configurations

The longitudinal ribs of the SRS gate were examined to evaluate their effectiveness in preventing excessive gate deflection under hydraulic loading. Figure 5a shows the four structural models used to compare the effects of longitudinal-rib number and gate plate thickness: 8EA-10 mm, 8EA-20 mm, 9EA-10 mm, and 10EA-10 mm. These cases were selected to examine the influence of rib quantity and plate thickness on the structural efficiency of the gate. Structural analysis was performed using MIDAS Civil. The reference gate geometry was 4978 mm in width and 2000 mm in height, while the comparative structural models varied the gate plate thickness between 10 and 20 mm according to the evaluated rib configuration.

The structural load was based on the governing hydraulic condition obtained from the three-dimensional flow analysis. The applied load consisted of the hydrostatic load, the component of the gate self-weight acting normal to the gate surface, and the flow-induced external force derived from the EFDC simulation. These load components were combined and converted into an equivalent static pressure load acting on the gate surface. A fixed restraint condition was applied at the actual anchor-bolt locations to idealize the kinematic restraint provided by the anchorage system during the static structural assessment. This boundary representation was adopted because the objective of the MIDAS Civil analysis was to evaluate the global response of the gate panel and longitudinal ribs under the prescribed hydraulic load, rather than to resolve local anchor deformation, bolt slip, or connection flexibility. These were therefore excluded from the finite-element model, while the anchor bolts were evaluated separately through the component-level safety checks

described in the following section. Figure 5b shows the corresponding load application and boundary-condition settings used in the structural model.

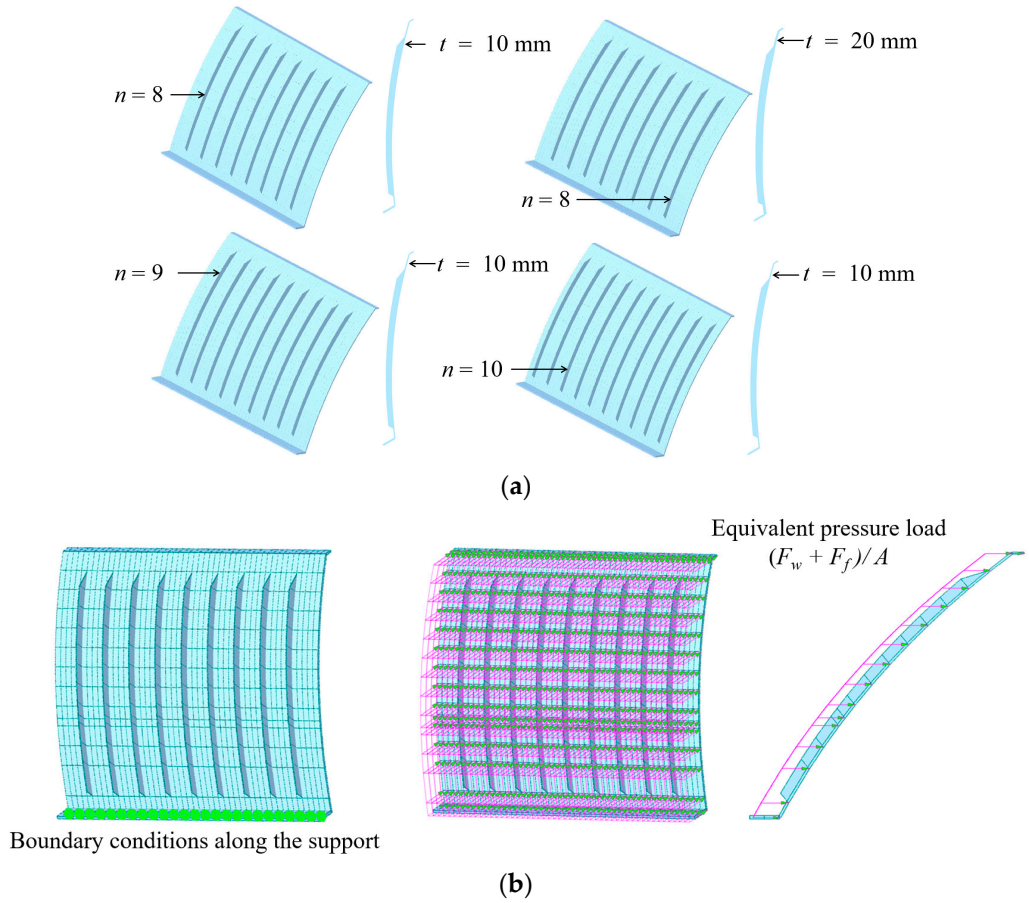


Figure 5. Structural models used for the SRS gate analysis: (**a**) longitudinal ribs and thickness configurations; (**b**) boundary conditions and applied load.

2.4. Component-Level Structural Safety Evaluation

After deriving the hydraulic and flow-induced loads, component-level safety checks were performed for the anchor bolts, clamping plates, and airbag of the SRS gate. These components were selected because selective gate operation can concentrate flow near lowered gate spans, increasing localized loading on the gate-support and sealing system.

2.4.1. Anchor Bolts

The anchor bolts were evaluated in terms of applied load and tensile stress. First, the total load acting on one gate span was converted into the load per unit gate width. Because five anchor bolts were considered for one gate span, the load acting on one anchor bolt was calculated as follows:

$$W_b = \frac{T_d}{n_b} \tag{5}$$

where W_b is the load acting on one anchor bolt (in kN), T_d is the total load ($F_w + F_g + F_f$) per 5.0 m gate width (in kN/m), and n_b is the number of anchor bolts (5EA). The safety factor against the applied load was calculated using the allowable bolt resistance:

$$SF_b = \frac{\sigma_{allow} A_b}{W_b} \tag{6}$$

where SF_b is the safety factor of the anchor bolt, σ_{allow} is the allowable stress of the bolt material taken as 21 kgf/mm^2, and A_b is the effective bolt area, set as 245 mm^2.

The tensile force acting at the bolt axis was considered as the sum of the tensile force induced by the design load and the tensile force caused by nut tightening:

$$R = R_1 + R_2 \tag{7}$$

where R is the total tensile force at the bolt axis (in kN), R_1 is the tensile force induced by the design load (in kN), and R_2 is the tensile force induced by nut tightening (in kN). The design-load-induced tensile force was calculated as follows:

$$R_1 = pW_b\left(\frac{L_1 + L_2}{L_2}\right) \tag{8}$$

where is p the anchor-bolt spacing (in m) and L_1 and L_2 are the distances from the anchor bolt to both ends of the clamping plate (in m). In the study, $p = 0.2$ m and $L_1 = L_2 = 0.09$ m were applied.

The tightening-induced tensile force was calculated from the conventional torque–preload relationship [26]:

$$R_2 = \frac{T}{dk} \times 1000 \tag{9}$$

where T is the tightening torque (in kN·m), k is the torque coefficient, and d is the nominal bolt diameter given by 24 mm. The tensile stress of the anchor bolt was then calculated as:

$$\sigma_b = \frac{R}{A_e} \tag{10}$$

where σ_b is the tensile stress in the anchor bolt (in MPa) and A_e is the effective cross-sectional area given by 3.53 cm^2. The tensile safety factor was calculated as:

$$SF_t = \frac{\sigma_u}{\sigma_b} \tag{11}$$

where σ_u is the reference failure stress of the bolt material, which was taken as 520 MPa corresponding to the tensile-strength level of STS304/Type 304 stainless steel.

For this study, a target safety factor of 3.0 was adopted as a conservative component-level screening criterion for the anchor-bolt checks. International anchorage design references emphasize that anchor systems should be evaluated with respect to relevant loading conditions and failure modes, including steel failure, concrete-related failure, pull-out, and combined actions [27]. Modern anchorage design frameworks generally use limit-state or partial-safety-factor formats rather than a single global safety factor [28]. However, an overall safety factor of 3.0 has also been used in allowable-stress-based anchor-bolt design practice to convert characteristic anchor resistance into design resistance [29]. Therefore, the adopted value of 3.0 was used only to screen the component-level safety of the SRS gate under the analyzed load cases and should not be interpreted as a replacement for project-specific code-based anchor design.

2.4.2. Clamping Plates

The clamping plates were evaluated against bending failure. The total bending moment acting on the clamping plate was calculated as the sum of the bending moment induced by nut tightening and the bending moment induced by the design tensile force:

$$M = M_a + M_b \tag{12}$$

where M is the total bending moment (in kN·cm), M_a is the bending moment due to nut tightening (in kN·cm), and M_b is the bending moment due to design tension (in kN·cm). The tightening-induced bending moment was calculated as:

$$M_a = \frac{R_2 L}{8} \tag{13}$$

where R_2 is the tightening-induced tensile force (in kN) and L is the width of the clamping plate (18 cm). The bending moment due to design tension was calculated as:

$$M_b = \frac{R_1 L}{4} \tag{14}$$

where R_1 is the tensile force induced by the design load (in kN). The maximum bending stress of the clamping plate was calculated using the conventional flexure relation [30] and the effective section modulus:

$$\sigma_{cp} = \frac{M}{Z} \tag{15}$$

$$Z = \frac{(B_{cp} - n_b D)t^2}{6} \tag{16}$$

$$\sigma_{cp} = \frac{6M}{(B_{cp} - n_b D)t^2} \tag{17}$$

where σ_{cp} is the maximum bending stress of the clamping plate (in MPa), Z is the effective section modulus (in cm^3), B_{cp} is the clamping-plate length (100 cm), n_b is the number of anchor bolts, D is the anchor-bolt diameter (2.4 cm), and t is the clamping-plate thickness (2.5 cm). This calculation represents a global bending-stress check of the clamping plate based on the effective net section after deducting the anchor-bolt openings. The nominal safety factor against permanent deformation of the clamping plate under global bending was calculated as:

$$SF_{cp} = \frac{\sigma_{u,cp}}{\sigma_{cp}} \tag{18}$$

where $\sigma_{u,cp}$ is the specified 0.2% proof strength of the Type 304 stainless-steel clamping plate, given by 210 MPa [31]. The resulting SF_{cp} therefore represents a nominal proof-strength-to-stress ratio for global bending. Similarly to the anchor-bolt assessment, a nominal safety factor of 3.0 was adopted as the screening criterion for the clamping-plate global bending assessment.

2.4.3. Airbag

The internal pressure of the airbag was evaluated to verify whether the airbag could resist the overturning action generated during SRS gate operation. The pressure was calculated by considering the overturning moments induced by the hydrostatic load, the gate self-weight component, and the flow-induced external force. Based on static moment equilibrium about the gate rotation axis [32], the required internal air pressure was determined as follows:

$$P = \frac{M_w + M_g + M_f}{J_1} \tag{19}$$

where P is the internal air pressure of the airbag (in MPa), M_w is the overturning moment caused by hydrostatic loading (in kN·m), M_g is the overturning moment caused by the gate self-weight component (in kN·m), M_f is the overturning moment caused by the flow-induced external force (in kN·m), and J_1 is the sectional first moment of the airbag-to-gate contact surface about the rotation axis (in m^3).

The sectional first moment of the contact surface was calculated as:

$$J_1 = \frac{\lambda {L_c}^2}{3} + \frac{(B - 2\lambda){L_c}^2}{2} \tag{20}$$

where L_c is the contact length between the airbag and the gate (in cm), B is the unit gate width (in cm), and λ is the length of the contactless region (in cm). This defines the first moment of the effective airbag-to-gate contact area about the gate rotation axis, which relates the internal air pressure to the resisting moment. A larger effective contact moment J_1 reduces the pressure required to balance a given overturning moment, whereas a larger contactless region reduces the effective contact contribution. The contactless length was calculated using:

$$\lambda = L_c cot\theta \tag{21}$$

$$\theta = 90^\circ - 0.75\alpha \tag{22}$$

where θ is the corner angle of the contact surface (in degrees) and α is the standing angle of the gate (in degrees). In this study, L_c= 12 cm, B = 500 cm, and $\alpha = 50^\circ$ were applied, giving $\theta = 53^\circ$ and λ = 9.21 cm.

The overturning moment caused by hydrostatic loading was calculated as:

$$M_w = \frac{\gamma_0 B\left(H^2 - {h_1}^2\right)(H + 2h_1)}{6(sin\alpha)^2} \tag{23}$$

where γ_0 is the unit weight of water (in kN/m^3), H is the design water depth (in m), h_1 is the overflow depth (in m), and α is the standing angle (in degrees). The overturning moment caused by the gate self-weight component was calculated as:

$$M_g = F_g L_g \tag{24}$$

where F_g is the component of the gate self-weight acting in the hydraulic-load direction (in kN) and L_g is the distance from the rotation center to the gate centroid (in m). The overturning moment caused by flow-induced loading was calculated as:

$$M_f = F_f L_f \tag{25}$$

where F_f is the flow-induced external force (in kN) and L_f is the distance from the rotation center to the point of action of the flow-induced force (in m).

The calculated internal air pressure was then compared with the reinforcing-fabric strength of the airbag to evaluate pressure resistance under the modeled gate-height conditions. For the airbag safety evaluation, the calculated internal air pressure, P, was compared with the reference reinforcing-fabric strength of the airbag, 180 kgf/cm^2 (or 17.65 MPa), which was used as the material-strength criterion in the design calculation. Public rubber-dam bladder specifications report tensile-strength requirements of the same order of magnitude, with tensile strength at break values commonly reported in the range of approximately 12–19 MPa depending on rubber layer, aging condition, and test condition.

2.5. Modeling Assumptions and Scope

The numerical framework was developed as a steady-state, one-way hydraulic-to-structural assessment. The EFDC analysis represented the ordinary-flow steady-state condition adopted for the original model, and the channel bed and banks were treated as fixed boundaries. Sediment transport, bed or bank deformation, and transient hydraulic pressure fluctuations were not included. Hydraulic loads derived from EFDC were trans-

ferred to MIDAS Civil as equivalent static structural loads, while structural deformation was not fed back to the hydraulic model. Accordingly, the fluid–solid interface was not explicitly resolved, and deformation-induced changes in the surrounding flow field and associated two-way fluid–structure interaction effects were outside the scope of the present analysis. The span-level flow-induced force was estimated by applying the maximum cell-level force over the corresponding gate span rather than by spatially integrating the non-uniform EFDC force distribution. Four operating scenarios were evaluated using raised and lowered gate configurations, while the intermediate gate motion associated with airbag inflation or deflation was not included in the reported numerical analysis. In addition, a formal grid-convergence analysis was not performed; therefore, the adopted discretization provides a common basis for scenario comparison but does not establish mesh independence of the absolute peak hydraulic quantities. Future numerical investigations should therefore include systematic grid-sensitivity and convergence analyses to quantify discretization uncertainty in the peak hydraulic quantities, together with transient gate-motion analysis to represent the transition between raised and lowered configurations during airbag inflation and deflation.

In the structural analysis, a fixed restraint condition was applied at the actual anchor-bolt locations as an idealized representation of the anchorage restraint for evaluating the global static response. Local support flexibility, bolt slip, and connection deformation were not explicitly represented and therefore remain outside the scope of the finite-element model. Similarly, the clamping-plate assessment was based on nominal global bending of the effective net section and did not explicitly account for bolt-hole stress concentrations, local bearing/contact stresses, or nonlinear bolt–plate interaction. The airbag–gate interface was not modeled through an explicit nonlinear contact formulation; consequently, friction and normal contact stiffness were not prescribed. Airbag resistance was instead evaluated separately through static moment equilibrium and comparison of the calculated internal-pressure demand with the reinforcing-fabric strength. Accordingly, the current study is a preliminary component-level static structural-safety assessment under the analyzed hydraulic conditions, providing a basis for structurally efficient, resource-conscious, and more sustainable design of river infrastructure.

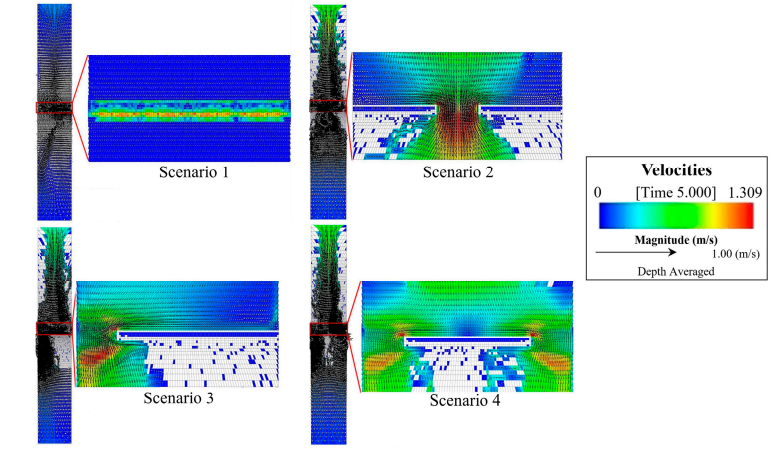
3. Results

This section presents the hydraulic and structural analysis results for the SRS movable weir under the evaluated gate-operation scenarios. The results include the EFDC-simulated flow patterns and velocity distributions, the external-force distributions derived from the hydraulic analysis, the structural response of the gate according to longitudinal-rib configuration, and the component-level safety evaluation of the anchor bolts, clamping plates, and airbag.

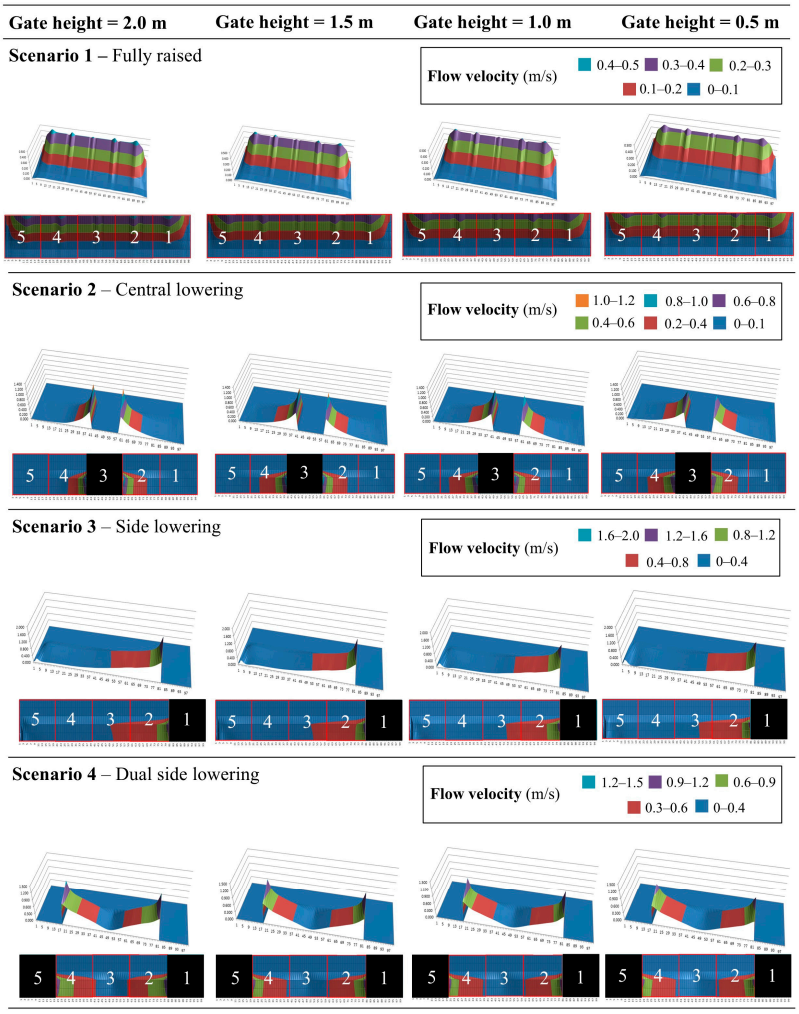
3.1. Flow Characteristics Under SRS Gate-Operation Scenarios

The EFDC simulation results shown in Figure 6 indicate that the gate-operation scenario strongly affected the flow pattern and velocity distribution near the SRS gate. Under Scenario 1, in which all five gates were fully raised, the upstream inflow was distributed across the channel width and overflowed over the SRS gate. After overflow, the flow rotated counterclockwise and exited downstream. The maximum overflow velocity decreased from 0.448 m/s at a gate height of 2.0 m to 0.363 m/s at a gate height of 0.5 m. Under Scenario 2, the upstream flow was concentrated toward the channel center and discharged through the lowered central span, Gate 3. The maximum velocity reached 1.153 m/s at a gate height of 2.0 m. Under Scenario 3, the upstream flow was concentrated toward the right bank and discharged through the lowered side span, Gate 1. This scenario

produced the highest maximum velocity among all evaluated cases, reaching 1.646 m/s at a gate height of 2.0 m. Under Scenario 4, the inflow was divided toward both side spans and discharged through lowered Gates 1 and 5, with a maximum velocity of 1.309 m/s at a gate height of 2.0 m.



(**a**)



(**b**)

Figure 6. EFDC simulation results showing: (**a**) flow fields; (**b**) gate-span velocity distributions under different SRS gate-operation scenarios. Numbers 1–5 indicate the individual SRS gates.

As summarized in Table 3, selective gate lowering changed the flow condition from distributed overflow to localized discharge through the lowered spans. Among the evaluated scenarios, Scenario 3 produced the most critical velocity condition and was therefore considered important for the subsequent external-force and structural safety evaluations.

Table 3. Summary of maximum velocity, velocity range, and within-span velocity difference for each gate-operation scenario and gate-height case.

Height (m)	Velocity Category	Scenario 1	Scenario 2	Scenario 3	Scenario 4
		(m/s)			
2.0	Range	0.007–0.448	0.002–1.153	0.022–1.646	0.029–1.309
	Maximum	0.448	1.153	1.646	1.309
	Within-span difference	0.441	1.151	1.624	1.280
1.5	Range	0.006–0.426	0.002–1.117	0.002–1.630	0.020–1.248
	Maximum	0.426	1.117	1.630	1.248
	Within-span difference	0.420	1.115	1.608	1.228
1.0	Range	0.006–0.412	0.002–1.067	0.014–1.484	0.013–1.231
	Maximum	0.412	1.067	1.484	1.231
	Within-span difference	0.406	1.065	1.470	1.218
0.5	Range	0.005–0.363	0.001–0.891	0.011–1.405	0.012–1.072
	Maximum	0.363	0.891	1.405	1.072
	Within-span difference	0.358	0.890	1.394	1.060

3.2. External Force Distribution Acting on the SRS Gate

The external-force distribution acting on the SRS gate was derived from the EFDC velocity field using the impulse–momentum-based procedure described in Section 2.2. The force distribution was evaluated for each gate-operation scenario and gate-height case to identify the gate spans most affected by localized flow concentration.

Figure 7 shows how the flow redistribution identified in Figure 7 was translated into localized external-force demand on the individual gate spans. Under the fully raised condition, the relatively distributed overflow produced a comparatively uniform force pattern across the five spans. Once selective lowering was introduced, the force distribution became strongly localized on the raised spans adjacent to the lowered gate. This behavior was most pronounced in Scenario 3, where side-gate lowering concentrated the flow near Gate 1 and produced the largest external force on the adjacent Gate 2. In Scenario 2, central lowering produced a more symmetric concentration on Gates 2 and 4, whereas dual-side lowering in Scenario 4 distributed the additional demand between the inner spans adjacent to the lowered side gates. These patterns indicate that the position of the lowered span governs not only the flow path but also the spatial transfer of hydraulic demand to neighboring gate components.

Although the maximum local external force occurred in Scenario 3 at a gate height of 1.5 m, this condition did not govern the subsequent structural analysis because the hydrostatic component increased with gate height; consequently, the 2.0 m condition produced the largest combined structural load. Figure 8 should therefore be interpreted as identifying the spatial concentration of flow-induced loading, whereas the governing structural case was determined from the combined hydrostatic, self-weight, and flow-induced load components.

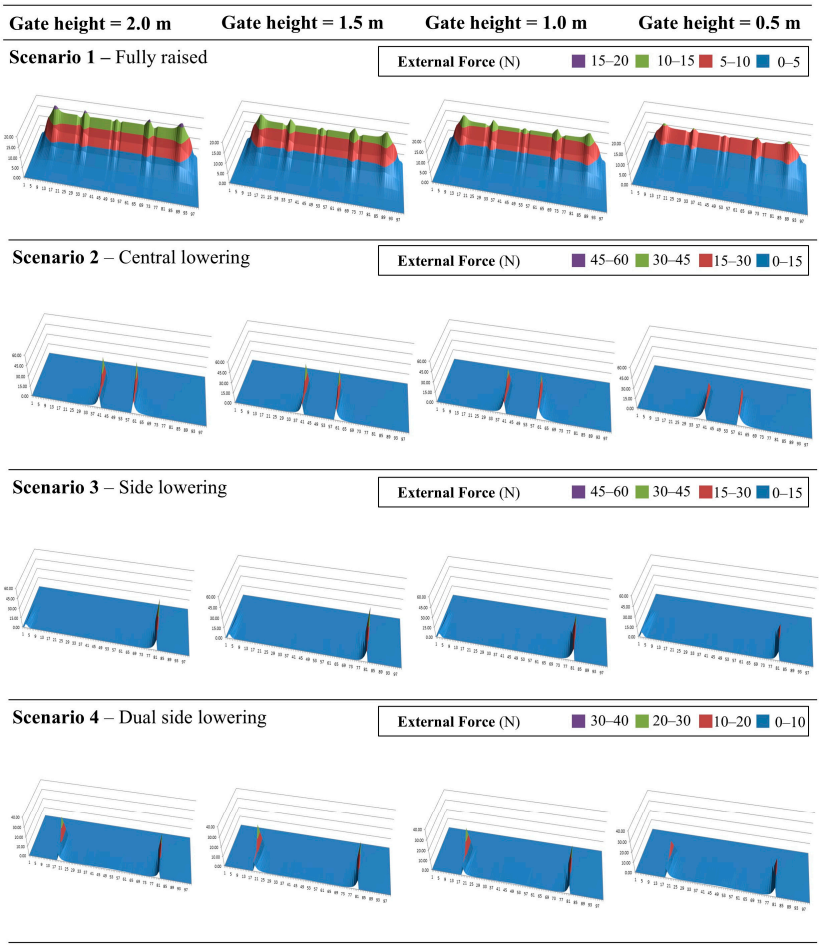


Figure 7. External force distributions acting on the SRS gate under the four gate-operation scenarios.

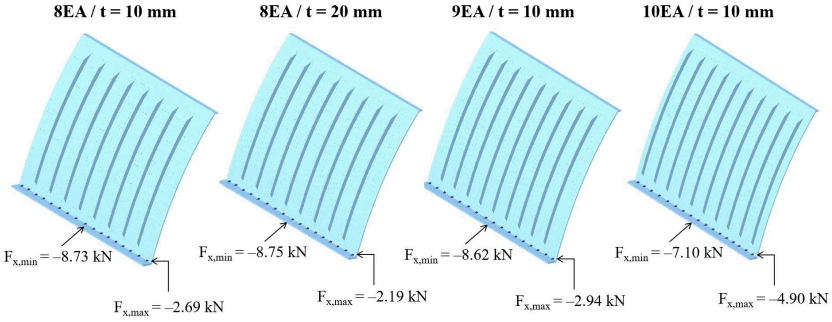


Figure 8. Reaction-force distributions for the four longitudinal-rib configurations.

The maximum external forces are presented in Table 4. Among the evaluated cases, Scenario 3 produced the largest maximum external force, with a maximum value of 50.88 N at a gate height of 1.5 m. Scenario 2 also produced a high maximum external force, reaching 47.24 N at a gate height of 2.0 m. In comparison, the fully raised condition in Scenario 1 showed substantially lower force differences across all gate-height cases.

The external-force results were then used to define the governing structural load for the subsequent rib-configuration analysis, as summarized in Table 5. Although Scenario 3 at a gate height of 1.5 m produced the largest local external force, the 2.0 m gate-height case produced the largest combined structural load because the hydrostatic load increased with gate height. Therefore, the 2.0 m gate-height condition was selected as the governing load case for the longitudinal-rib analysis. For this case, the hydrostatic load, self-weight component in the hydraulic-load direction, and flow-induced external force were 179.10,

2.20, and 4.94 kN, respectively, resulting in a total load of 186.25 kN. The distributed pressure load applied to the gate surface in the structural model was calculated using the hydrostatic (F_w) and flow-induced components (F_f), divided by the applied sectional area of 13.5 m^2, giving 13.63 kN/m^2.

Table 4. Summary of maximum external forces.

Scenario	Height (m)	Gate 1	Gate 2	Gate 3	Gate 4	Gate 5
				(N)		
1	2.0	16.25	16.08	15.70	16.08	16.25
	1.5	14.67	14.51	13.36	14.51	14.67
	1.0	13.76	13.61	12.60	13.61	13.76
	0.5	10.66	10.55	9.91	10.47	10.66
2	2.0	0.02	47.24	–	46.73	0.07
	1.5	0.13	46.88	–	46.40	0.10
	1.0	0.16	38.30	–	37.33	0.12
	0.5	0.21	23.76	–	23.56	0.20
3	2.0	–	49.42	0.14	0.12	5.65
	1.5	–	50.88	0.15	0.12	6.47
	1.0	–	39.16	0.25	0.19	6.56
	0.5	–	24.76	0.31	0.29	8.04
4	2.0	–	27.09	0.97	28.46	–
	1.5	–	29.16	0.58	30.18	–
	1.0	–	28.46	0.76	29.43	–
	0.5	–	17.92	1.08	18.28	–

Table 5. Governing load combination used for structural analysis.

	Value
Hydrostatic Load, F_w (kN)	179.10
Self-weight component in hydraulic-load direction, F_g (kN)	2.20
Flow-induced external force, F_f (kN)	4.94
Total load, $F_w + F_g + F_f$ (kN)	186.25
Applied sectional area, A (m^2)	13.50
Distributed pressure load, $(F_w + F_f)/A$ (kN/m^2)	13.63

The flow-induced force was estimated by applying the maximum cell-level force over the corresponding gate span. Because the EFDC results showed a spatially non-uniform velocity distribution, the associated hydraulic loading was also non-uniform and was not explicitly integrated in this calculation. Applying the local maximum across the evaluated span may therefore overestimate the span-averaged flow-induced contribution. However, as shown in Table 5, the flow-induced component accounts for only approximately 2.7% of the governing total load, which is dominated by hydrostatic loading. Accordingly, this simplification mainly affects the comparatively small flow-induced contribution rather than the dominant component of the static load combination. Direct cell-wise integration or area-weighted averaging would provide a more representative estimate in future analyses.

3.3. Effect of Longitudinal-Rib Configuration on Structural Response

The structural response of the SRS gate was evaluated for the four longitudinal-rib configurations. The structural response was evaluated using reaction force, bending moment, displacement, and stress as the principal response quantities [33]. These responses were used to determine whether increasing the number of longitudinal ribs or increasing the gate thickness provided a more efficient improvement in structural performance.

Figure 8 shows the reaction-force distributions for the four configurations. The 8EA-10 mm and 8EA-20 mm models showed similar maximum reaction levels, whereas the 9EA-10 mm and 10EA-10 mm models redistributed the reaction more effectively along the lower support region. In particular, the 10EA-10 mm model produced the lowest maximum reaction force among the evaluated configurations, indicating that the additional rib improved load distribution along the gate-support line.

Figure 9 presents the bending-moment distributions in the M_{xx} and M_{yy} directions. The 8EA/t = 10 mm configuration produced the largest moment demand, with maximum M_{xx} and M_{yy} values of 5.11 and 3.80 kN·m/m, respectively. Increasing the plate thickness from 10 mm to 20 mm in the 8EA model reduced the maximum M_{xx} moment to 3.52 kN·m/m, but this improvement was achieved by increasing the plate thickness rather than by improving rib layout. For the 10 mm thick gate models, increasing the rib number from 8EA to 9EA and 10EA reduced the M_{yy} demand from 3.80 to 2.64 and 2.27 kN·m/m, respectively, showing that additional longitudinal ribs improved the distribution of bending demand in the transverse direction. This trend is consistent with the general structural role of stiffeners in steel plate systems, where stiffener layout affects bending response, local stress concentration, and deformation control [34,35].

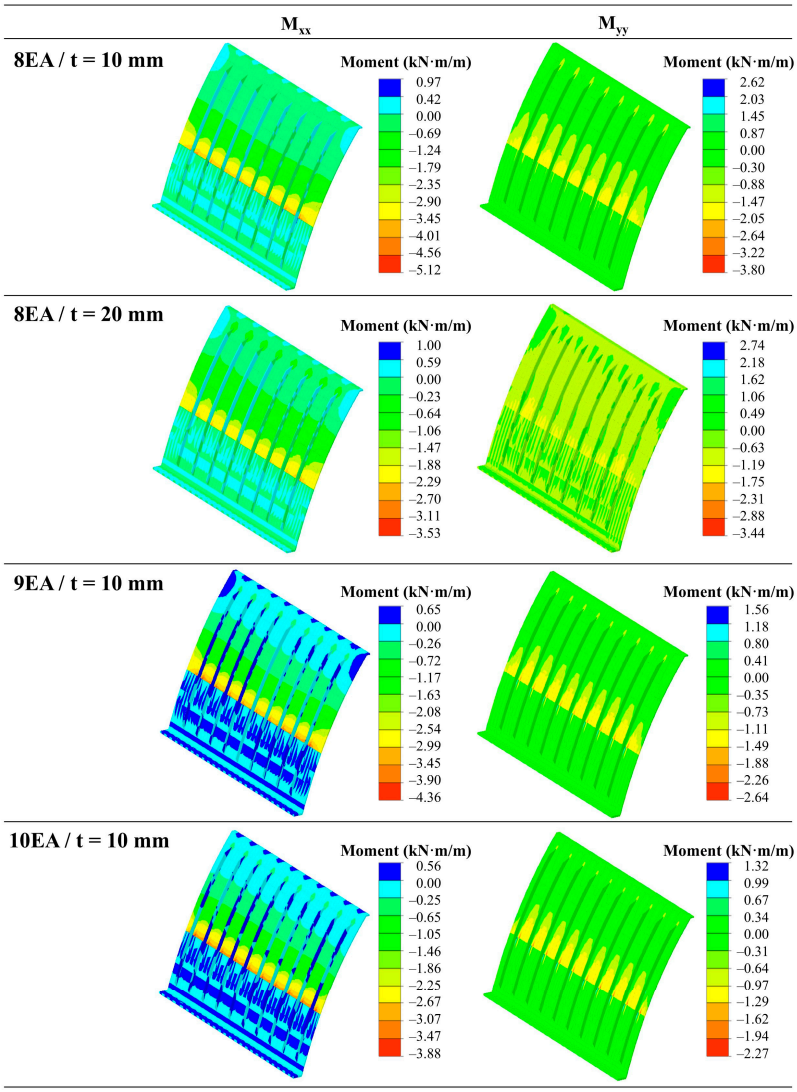


Figure 9. Bending-moment distributions of the SRS gate for different longitudinal-rib and plate-thickness configurations.

The displacement and stress results are shown in Figure 10. The maximum z-direction displacement was 17.58 mm for 8EA-10 mm, 10.92 mm for 8EA-20 mm, 15.97 mm for 9EA-10 mm, and 13.51 mm for 10EA-10 mm. The corresponding maximum stresses were 309.54, 179.49, 281.97, and 246.28 MPa, respectively. The lower stress and displacement observed in the 8EA-20 mm configuration are expected in a mechanical sense, because plate flexural rigidity is strongly governed by thickness [36,37]. However, the 9EA-10 mm and 10EA-10 mm configurations also improved the structural response by increasing the rib count while maintaining the original plate thickness, thereby avoiding the additional material demand associated with plate thickening.

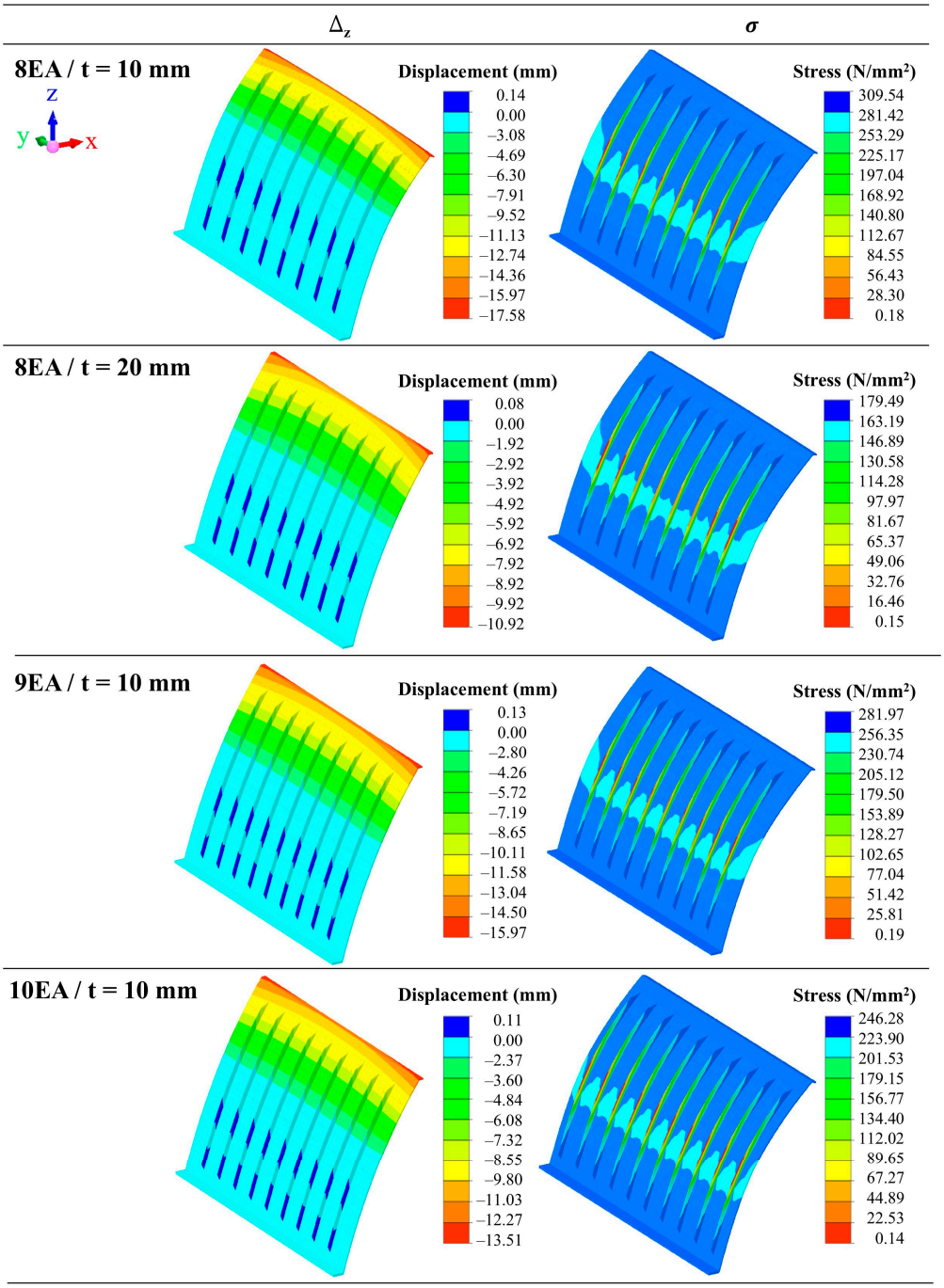


Figure 10. Z-direction displacement and stress distributions of the SRS gate for different longitudinal-rib and plate-thickness configurations.

All configurations satisfied the material stress criterion when compared with the 345 MPa yield strength of ASTM A572 Grade 50 steel [38]. To compare how close each configuration was to the material limit, the stress utilization ratio was calculated by:

$$U_s = \frac{\sigma_{max}}{F_y} \times 100\ (\%) \quad (26)$$

where σ_{max} is the maximum stress (in MPa) and F_y is the yield strength (in MPa). The 8EA-10 mm configuration showed the highest stress utilization, reaching 89.72% of the reference strength, leaving only 10.28% remaining stress reserve. In structural-steel design assessment, utilization ratio is commonly used to express how close a member is to its capacity, and lower excess capacity can indicate less available design reserve [39]. Therefore, although the 8EA-10 mm model satisfied the stress criterion, it was not selected as the preferred configuration because it provided the smallest remaining stress reserve among the evaluated cases. The 8EA-20 mm configuration provided the lowest stress and displacement, but this improvement was achieved by doubling the plate thickness. As summarized in Table 6, among the 10 mm thick configurations, the 9EA-10 mm configuration reduced both stress and displacement compared with 8EA-10 mm while requiring fewer ribs than 10EA-10 mm. Additionally, because engineering design selection often involves multiple competing criteria rather than a single minimum-response value [40], 9EA-10 mm was considered a balanced configuration in terms of stress safety, displacement control, and rib-material efficiency.

Table 6. Summary of structural responses according to longitudinal-rib configuration.

Configuration	Max. Reaction (kN)	$M_{xx,max}$ (kN·m/m)	$M_{yy,max}$ (kN·m/m)	$D_{z,max}$ (mm)	σ_{max} (MPa)	U_s (%)
8EA-10 mm	8.78	5.11	3.80	17.58	309.54	89.72
8EA-20 mm	8.75	3.52	3.44	10.92	179.49	52.03
9EA-10 mm	8.62	4.36	2.64	15.97	281.97	81.73
10EA-10 mm	7.10	3.87	2.27	13.51	246.28	71.39

3.4. Component-Level Structural Safety

3.4.1. Anchor Bolt Safety

The anchor-bolt safety evaluation was performed by converting the total load acting on one gate span into the design load per unit gate width and then into the load applied to one anchor bolt. The load conversion results are summarized in Table 7. The total load acting on one gate span decreased from 186.25 kN at a gate height of 2.0 m to 25.47 kN at a gate height of 0.5 m. Accordingly, the applied load per anchor bolt decreased from 7.45 to 1.02 kN. The safety factor against the applied anchor-bolt load exceeded 3.0 for all gate-height cases, ranging from 6.77 to 49.49, indicating that the anchor bolts had sufficient resistance against the applied load.

Table 7. Load conversion for anchor bolt safety evaluation.

Gate Height (m)	Total Load F_w+F_g+F_f (kN)	Unit-Length Total Load, T_d (kN/m)	Applied Load per Anchor Bolt, W_b (kN)	S.F. Against Applied Load, SF_b
2.0	186.25	37.25	7.45	6.77
1.5	117.63	23.53	4.71	10.72
1.0	63.69	12.74	2.55	19.79
0.5	25.47	5.09	1.02	49.49

The anchor-bolt tensile-force check was performed by considering both the tensile force induced by the design load and the tensile force caused by nut tightening, as summarized in Table 8. This approach is appropriate because anchor bolts in concrete-supported systems are commonly evaluated against tensile and pull-out-related failure modes, and safety-factor-based verification is required to ensure anchorage reliability under applied loading [41]. The tensile force induced by the design load, R_1, decreased from 2.98 kN at a gate height of 2.0 m to 0.41 kN at a gate height of 0.5 m, while the tightening-induced tensile force, R_2, remained constant at 49 kN (5000 kgf) since the same tightening conditions were applied. This is consistent with bolted-joint mechanics, where tightening torque is related to bolt preload through the bolt diameter and nut factor/torque coefficient [42]. As a result, the total tensile force at the bolt axis ranged from 51.98 to 49.41 kN. The resulting tensile stress decreased from 147.25 to 139.96 MPa, and the tensile safety factor ranged from 3.53 to 3.71. Therefore, the anchor bolts satisfied both the applied-load and tensile-stress checks.

Table 8. Anchor bolt tensile force safety factors according to gate height.

	Gate Height (m)			
	2.0	**1.5**	**1.0**	**0.5**
Tensile force induced by load, R_1 (kN)	2.98	1.88	1.02	0.41
Tensile force induced by tightening, R_2 (kN)	49.00	49.00	49.00	49.00
Total anchor-bolt tensile force, R (kN)	51.98	50.88	50.02	49.41
Tensile stress, σ_b (MPa)	147.25	144.14	141.70	139.96
Tensile safety factor, SF_t	3.53	3.60	3.67	3.71

3.4.2. Clamping-Plate Safety

The clamping-plate safety check was performed by evaluating the bending moment and bending stress generated by nut tightening and design tension, as summarized in Table 9. This check is necessary because clamped plates in bolted joints can experience bending deformation and stress redistribution under external axial load or bending moment, and their response is influenced by bolt tightening, contact state, and plate stiffness [43]. The nut tightening bending moment, M_a, remained constant at 110.25 kN·cm for all gate-height cases because the same tightening condition was applied. In contrast, the bending moment induced by design tension, M_b, decreased from 13.41 kN·cm at a gate height of 2.0 m to 1.83 kN·cm at a gate height of 0.5 m. Consequently, the total bending moment, M, decreased from 123.66 to 112.08 kN·cm. The corresponding maximum bending stress, σ_{cp}, ranged from 13.49 to 12.23 MPa, and the safety factor, SF_{cp}, ranged from 15.57 to 17.17. These values indicate that the clamping plate satisfied the adopted nominal global bending criterion under all evaluated gate-height conditions. The comparatively large reserve against global bending suggests that future optimization of the clamping-plate thickness may be possible; however, the present calculation does not account for bolt-hole stress concentrations, local bearing/contact stresses, or nonlinear bolt–plate interaction. These local effects should therefore be examined in future work using detailed contact-based finite-element modeling or experimental validation.

Table 9. Clamping-plate safety factors according to gate height.

	Gate Height (m)			
	2.0	**1.5**	**1.0**	**0.5**
Nut-tightening bending moment, M_a (kN·cm)	110.25	110.25	110.25	110.25
Design tension bending moment, M_b (kN·cm)	13.41	8.47	4.59	1.83

Table 9. *Cont.*

	Gate Height (m)			
	2.0	**1.5**	**1.0**	**0.5**
Total bending moment, M (kN·cm)	123.66	118.72	114.84	112.08
Maximum bending stress, σ_{cp} (MPa)	13.49	12.95	12.53	12.23
Safety factor, SF_{cp}	15.57	16.22	16.76	17.17

3.4.3. Airbag Internal Pressure

The airbag internal-pressure check was performed by calculating the overturning moments induced by hydrostatic load, gate self-weight, and flow-induced external force, and then estimating the internal air pressure required to resist these moments. This check is important because inflatable rubber-dam systems are governed by the interaction between internal pressure, external water head, overflow condition, and structural deformation [44]. Previous numerical and experimental studies on rubber dams have also shown that internal pressure and upstream water level strongly affect the equilibrium shape and load-resisting behavior of inflatable dam bodies [45,46].

The calculated airbag internal-pressure results are summarized in Table 10. The hydrostatic overturning moment, M_w, decreased from 2.50 kN·m at a gate height of 2.0 m to 0.15 kN·m at a gate height of 0.5 m. The self-weight-induced overturning moment, M_g, remained constant at 0.02 kN·m, while the flow-induced overturning moment, M_f, decreased from 0.06 to 0.01 kN·m. Consequently, the total overturning moment decreased from 2.57 to 0.18 kN·m, and the calculated internal air pressure, P, decreased from 0.073 to 0.005 MPa. These values remained substantially below the adopted reinforcing-fabric strength of 17.65 MPa, indicating sufficient airbag resistance under all evaluated gate-height conditions.

Table 10. Airbag overturning moment and internal pressure according to gate height.

	Gate Height (m)			
	2.0	**1.5**	**1.0**	**0.5**
Hydrostatic overturning moment, M_w (kN·m)	2.50	1.30	0.55	0.15
Self-weight overturning moment, M_g (kN·m)	0.02	0.02	0.02	0.02
Flow-induced overturning moment, M_f (kN·m)	0.06	0.05	0.03	0.01
Total overturning moment, $M_w + M_g + M_f$ (kN·m)	2.57	1.36	0.60	0.18
Internal air pressure, P (MPa)	0.073	0.039	0.017	0.005

4. Discussion

4.1. Effect of Selective Gate Operation on Flow Concentration

Selective gate operation substantially altered the spatial distribution of flow across the SRS weir, with the strongest concentration occurring when a single side gate was lowered. Relative to the fully raised condition, side-gate lowering produced approximately a 267% increase in maximum velocity at the 2.0 m gate height. These results indicate that selective operation cannot be represented adequately by uniformly raised or symmetrically operated gate conditions because the location of the lowered span governs the resulting hydraulic response.

The pronounced response in Scenario 3 can be attributed to the asymmetric hydraulic condition created when a single side gate is lowered. Unlike central lowering, where approaching flow can converge toward the opening from both sides, side lowering generates an asymmetric cross-channel contraction that redirects flow toward a bank-adjacent opening. The resulting jet is bounded by the riverbank on one side and an adjacent raised gate on the other, thereby restricting lateral redistribution and producing steep transverse velocity gradients near the side span. This hydraulic mechanism also explains why the gate adjacent to the lowered side span was identified as the governing structural case in the

subsequent load assessment. Accordingly, Scenario 3 represents a coupled hydraulic and structural design condition rather than merely the scenario with the highest local velocity.

The hydraulic trends obtained in the present analysis are consistent with published experimental and numerical studies of movable gates. Particle image velocimetry (PIV) experiments on a rising-sector gate showed that gate opening substantially alters the local velocity distribution and produces concentrated velocities near the gate opening [13]. Similarly, combined experimental and numerical analysis of a multi-plate rotary gate demonstrated that changes in gate configuration redistribute both the flow field and the hydraulic force acting on individual gate plates [14]. Together, these studies demonstrate gate-operation-dependent redistribution of velocity and hydraulic demand similar to that observed among the SRS spans. However, because the gate geometry, scale, operating mechanism, and hydraulic boundary conditions differ among these studies, the comparison supports the general consistency of the present EFDC results with previous findings rather than direct validation of the model.

The bank-adjacent concentration observed in Scenario 3 may also have implications beyond the structural response of the gate. Near-bank velocity and boundary shear stress are important controls on sediment entrainment and channel adjustment [47], while experimental studies of gated hydraulic structures have demonstrated that concentrated and asymmetric flow can promote localized scour downstream of the opening [48,49]. In the present case, the combination of a bank-adjacent jet, restricted lateral redistribution, and steep transverse velocity gradients under side-gate lowering suggests that repeated operation of this scenario may increase scour susceptibility near the adjacent bank, downstream bed, or apron edge. This implication is particularly relevant where the bed or bank material is readily erodible or where local protection is limited. Because scour magnitude was not directly simulated in the present study, the observed hydraulic concentration should be interpreted as an indicator of potential scour susceptibility rather than as a prediction of erosion depth. To determine whether this hydraulic concentration translates into significant morphological change, repeated-operation effects should be evaluated through morphodynamic modeling or physical experiments.

4.2. Material-Efficient Rib Configuration for SRS Gate Design

The comparison of rib configurations indicates that structural improvement can be achieved through two fundamentally different design strategies: increasing plate thickness or improving stiffener arrangement. Plate thickening increases flexural rigidity directly, but it also increases steel demand throughout the gate panel. By contrast, additional longitudinal ribs redistribute bending demand while retaining the original plate thickness. The latter approach is therefore particularly relevant where structural efficiency must be balanced against material use. This result agrees with the general behavior of stiffened steel plate systems, where stiffener arrangement influences local deformation, buckling resistance, and stress distribution. Studies on longitudinally stiffened plates and stiffened steel plate systems have similarly shown that stiffener layout and stiffness affect plate response and can be evaluated through numerical or finite-element-based analysis [35,50,51]. The stress distributions observed in the present analysis also indicate that local buckling should be considered when evaluating the longitudinal-rib configurations. Previous studies have shown that the buckling response of longitudinally stiffened plates is governed by stiffener stiffness, spacing, boundary restraint, and interactions among local, distortional, and global deformation modes [51,52]. In the present results, increasing the rib number reduced stress and displacement and improved load redistribution; however, these trends alone do not establish the buckling resistance of the ribs or adjacent plate regions. Dedicated eigenvalue and geometrically nonlinear buckling analyses incorporating initial imperfections are

therefore needed to quantify critical loads and associated buckling modes. Additionally, a previous specialized stiffened-plate optimization considered plate thickness, stiffener number, and stiffener spacing as design variables for reducing structural weight while satisfying mechanical performance requirements, supporting the use of rib-layout modification as a material-efficient alternative to simple plate thickening [18]. Therefore, future studies should further investigate optimized rib spacing, rib geometry, and rib–plate configurations to reduce steel demand while maintaining the required stress, displacement, and safety performance of SRS gates.

From a sustainability perspective, this selection is meaningful because material efficiency is increasingly recognized as a key strategy for reducing embodied carbon in structural systems. It has been reported that designing structural steel for minimum material use, rather than only minimum cost, can reduce steel consumption and associated embodied carbon [39]. In recent studies, it has also been emphasized that material quantities and embodied carbon are closely linked, and that material efficiency is an important design lever for reducing embodied carbon in structural systems [53]. Although the present study did not perform a life-cycle carbon assessment, avoiding unnecessary plate-thickness increase or excessive rib addition while satisfying stress and displacement requirements is consistent with sustainability-oriented structural design. Future studies should also quantify this potential benefit through life-cycle assessment and cost–carbon optimization of alternative rib layouts under different hydraulic loading and operational conditions.

4.3. Component-Level Safety and Service Life Implications

The component-level safety checks provide an important link between hydraulic–structural performance and sustainability-oriented operation of the SRS gate. For movable hydraulic structures, satisfactory global gate response alone does not fully demonstrate safe operation, because load transfer is ultimately governed by connection and support components such as anchor bolts, clamping plates, and airbag systems. International anchorage design guidance also emphasizes that anchor systems should be evaluated with respect to relevant loading conditions and failure modes, including steel failure, pull-out, concrete-related failure, and combined actions [27]. Therefore, the component-level checks performed in this study are important for confirming that selective gate operation does not create localized component demands that could lead to premature repair or replacement.

From a life-cycle perspective, the component-level safety results are relevant because the sustainability of hydraulic infrastructure is affected not only by initial material quantities but also by service life, maintenance demand, repair frequency, and component replacement. Life-cycle studies on dams and hydropower infrastructure commonly define environmental impacts across construction, operation, maintenance, and end-of-life stages, showing that maintenance and repair activities should be considered when evaluating long-term infrastructure performance [20,54]. In this context, verifying the safety of the anchor bolts, clamping plates, and airbag is not only a structural requirement but also a way to support longer service life and reduce avoidable maintenance associated with localized component failure.

The anchor-bolt results showed that both the applied-load and tensile-stress checks satisfied the target safety criterion under all evaluated gate-height conditions. This indicates that the load transferred from the gate to the support system remained within the evaluated component capacity. The airbag results also showed that the calculated internal pressure was far below the reinforcing-fabric strength, indicating that internal-pressure demand was not critical under the analyzed hydraulic conditions. These results support the structural feasibility of selective gate operation, because the system maintained component-level safety even when hydraulic loading became locally concentrated around lowered and adjacent raised spans.

The relatively high clamping-plate safety factors indicate that global bending failure was not the governing limit state for this component. From a sustainable design perspective, this suggests that the clamping plate may have potential for future material optimization, provided that other limit states such as bolt-hole stress concentration, local bearing, contact pressure, fatigue, corrosion allowance, and constructability requirements are also satisfied. Previous studies on structural material efficiency have shown that reducing material use from unused capacity can contribute to lower steel consumption and embodied carbon in structural systems [39,53]. Therefore, future studies should examine optimized clamping-plate dimensions using detailed contact-based finite-element analysis and life-cycle assessment to quantify the trade-off between structural safety, fabrication requirements, and material-related environmental impact.

The present static checks also highlight several mechanisms that require separate evaluation before long-term service performance can be established. In particular, repeated operation, local contact behavior, fatigue, preload variation, and time-dependent material degradation were not analyzed in the present static safety assessment. Accordingly, the current component checks should be interpreted only as static strength assessments and not as predictions of component service life. Future work should therefore extend the component-level assessment beyond static safety-factor checks by examining local stress concentrations and contact behavior around the anchor and clamping regions, fatigue and preload variation under repeated selective gate operation, and airbag durability associated with repeated inflation–deflation, abrasion, aging, reinforcing-fabric degradation, and long-term airtightness. In addition, component-level life-cycle assessment and cost–carbon optimization should be conducted to determine whether reductions in plate dimensions, anchor-bolt layout, or airbag material specifications can reduce material demand and maintenance-related environmental impacts while maintaining structural safety.

5. Conclusions

This study evaluated the structural safety of an SRS movable weir under selective gate-operation conditions by combining EFDC-based hydraulic analysis with structural and component-level safety assessment. The principal findings and design implications are summarized as follows:

- Selective gate operation produces strongly non-uniform hydraulic loading, with flow concentration extending beyond the lowered span to adjacent raised gates. Accordingly, segmented movable-weir design should consider span-specific loading rather than assuming uniform hydraulic demand across the structure.
- The critical hydraulic demand occurred in the side-gate lowering scenario, where asymmetric gate operation concentrated the flow near the lowered side span and produced the maximum external-force condition.
- Structural efficiency can be improved through stiffener arrangement without relying solely on increased plate thickness. The present rib comparison indicates that redistributing stiffness through additional longitudinal ribs can reduce stress and deformation while limiting additional plate material. Accordingly, rib layout and plate thickness should be optimized together when material efficiency is a design objective.
- Global gate safety should be complemented by component-level verification of the load-transfer path. Anchor bolts, clamping plates, and airbag systems should be evaluated separately because satisfactory global gate response does not by itself demonstrate adequate resistance of individual connection and support components.
- The results support the structural feasibility of selective SRS operation under the investigated static hydraulic conditions, while broader application requires consideration of

site-specific hydraulic conditions, connection behavior, repeated operation, durability, and numerical uncertainty.

Although the coupled EFDC–MIDAS framework extends approaches that consider hydraulic or structural behavior separately by linking scenario-specific flow redistribution with structural and component-level response, several methodological limitations remain. The present framework relies on steady-state one-way hydraulic-to-structural load transfer, simplified contact and anchorage representations, and does not include formal grid-convergence verification, sediment morphodynamics, or experimental validation. These limitations can be addressed through systematic mesh-sensitivity analysis, spatial integration of hydraulic loads, transient two-way fluid–structure interaction, nonlinear contact modeling, and physical or field validation. Future investigations should further examine scour under repeated selective operation, fatigue and anchor-preload variation, airbag aging, abrasion and airtightness degradation, and long-term field performance. Life-cycle assessment and cost–carbon optimization should also be incorporated to establish site-specific design and maintenance strategies that balance structural safety, material efficiency, durability, and environmental performance.

Author Contributions: Conceptualization: M.S.K., J.-H.K., C.-G.P. and J.Y.; Data Curation: J.-H.K. and S.-J.L.; Formal Analysis: M.S.K., J.-H.K. and C.-G.P.; Funding Acquisition: C.-G.P.; Investigation: M.S.K., S.-J.L. and C.-G.P.; Methodology: M.S.K., J.-H.K., S.-J.L. and J.Y.; Project Administration: C.-G.P.; Resources: J.-H.K. and J.Y.; Software: M.S.K. and S.-J.L.; Supervision: J.Y.; Validation: D.G.S. and S.-J.L.; Visualization: D.G.S. and S.-J.L.; Writing—Original Draft Preparation: M.S.K., J.-H.K. and C.-G.P.; Writing—Review and Editing: D.G.S. and J.Y. All authors have read and agreed to the published version of the manuscript.

Funding: This work was supported by Korea Institute of Planning and Evaluation for Technology in Food, Agriculture and Forestry (IPET) through Intelligent Agricultural Infra Management for Climate Change Development Program, funded by Ministry of Agriculture, Food and Rural Affairs (MAFRA) (RS-2025-02219948).

Institutional Review Board Statement: Not applicable.

Informed Consent Statement: Not applicable.

Data Availability Statement: The raw data supporting the conclusions of this article will be made available by the authors on request.

Conflicts of Interest: The authors declare no conflicts of interest.

Abbreviations

The following abbreviations are used in this manuscript:

SRS	Smart rubber and steel
EFDC	Environmental Fluid Dynamics Code
WAMIS	Water Resources Information System
PIV	Particle image velocimetry
STS304	Type 304 stainless steel
S.F.	Safety factor
EL.	Elevation

References

1. Shih, S.-S.; Liu, C.-H.; Ning, J.-H. In-River Weir Effects on the Alteration of Flow Regime and Regarding Structural Stream Habitat. *J. Hydrol.* **2022**, *615*, 128670. [CrossRef]
2. Csiki, S.; Rhoads, B.L. Hydraulic and Geomorphological Effects of Run-of-River Dams. *Prog. Phys. Geogr.* **2010**, *34*, 755–780. [CrossRef]

3. Nilsson, C.; Reidy, C.A.; Dynesius, M.; Revenga, C. Fragmentation and Flow Regulation of the World's Large River Systems. *Science* **2005**, *308*, 405–408. [CrossRef] [PubMed]
4. Grill, G.; Lehner, B.; Thieme, M.; Geenen, B.; Tickner, D.; Antonelli, F.; Babu, S.; Borrelli, P.; Cheng, L.; Crochetiere, H.; et al. Mapping the World's Free-Flowing Rivers. *Nature* **2019**, *569*, 215–221. [CrossRef] [PubMed]
5. Jones, J.I.; Murphy, J.F.; Collins, A.L.; Sear, D.A.; Naden, P.S.; Armitage, P.D. The Impact of Fine Sediment on Macro-Invertebrates. *River Res. Appl.* **2012**, *28*, 1055–1071. [CrossRef]
6. Owens, P.N.; Batalla, R.J.; Collins, A.J.; Gomez, B.; Hicks, D.M.; Horowitz, A.J.; Kondolf, G.M.; Marden, M.; Page, M.J.; Peacock, D.H.; et al. Fine-Grained Sediment in River Systems: Environmental Significance and Management Issues. *River Res. Appl.* **2005**, *21*, 693–717. [CrossRef]
7. Kemp, P.; Sear, D.; Collins, A.; Naden, P.; Jones, I. The Impacts of Fine Sediment on Riverine Fish. *Hydrol. Process.* **2011**, *25*, 1800–1821. [CrossRef]
8. Niu, D.; Li, Y.; Tan, Y.; Ma, C.; Qi, Y.; Li, Y.; Tang, J. The Impact of Water-Sediment Regulation Scheme (WSRS) on the Chemistry of Dissolved Organic Matter in the Yellow River Estuary and Adjacent Waters. *Water Res.* **2025**, *282*, 123669. [CrossRef]
9. Casserly, C.M.; Turner, J.N.; O' Sullivan, J.J.; Bruen, M.; Bullock, C.; Atkinson, S.; Kelly-Quinn, M. Effect of Low-Head Dams on Reach-Scale Suspended Sediment Dynamics in Coarse-Bedded Streams. *J. Environ. Manag.* **2021**, *277*, 111452. [CrossRef]
10. Yoo, S.-Y.; Jeon, J.-C.; Shin, H.-J.; Park, C.-G. Environmental Exposure Performance of a Panel-Type Glass-Fiber-Reinforced Polymer Composite Clamping Plate for an Improved Moveable Weir. *J. Korean Soc. Agric. Eng.* **2017**, *59*, 73–81. [CrossRef]
11. Ministry of Land, Infrastructure and Transport (MOLIT). *Development of an Advanced Hybrid Movable Weir Combining GFRP and Steel Materials for Multipurpose Applications: Final Report of the Second-Year Land, Infrastructure and Transport Technology Commercialization Support Program*; 15TBIP-C072924-02; Korea Agency for Infrastructure Technology Advancement (KAIA): Anyang, Republic of Korea, 2016.
12. Erdbrink, C.D.; Krzhizhanovskaya, V.V.; Sloot, P.M.A. Free-Surface Flow Simulations for Discharge-Based Operation of Hydraulic Structure Gates. *J. Hydroinform.* **2014**, *16*, 189–206. [CrossRef]
13. Song, C.G.; Park, S.W.; Shin, J. An Experimental Study of Flow and Turbulence Properties near the Rising Sector Gate Mouth Considering the Gate Opening with a PIV Measuring System. *Water* **2024**, *16*, 3004. [CrossRef]
14. Qi, H.; Zhang, X.; Sun, Y.; Ji, X.; Tian, D.; Sun, C.; Xue, Z.; Liu, Y. Research on Flow Field Characteristics of a Three-Plate Vertical Rotary Gate. *Water* **2025**, *17*, 456. [CrossRef]
15. Hu, H.; Wang, X.; Bao, Y.; Zuo, Y.; Zhang, P.; Qi, Q.; Deng, H. Transient Analysis of Cylindrical Shells via a Numerically Stable Discrete Time State Space Technique. *Thin-Walled Struct.* **2026**, *231*, 115357. [CrossRef]
16. Bao, Y.; Wang, X.; Hu, H.; Zuo, Y.; Tu, S.; Zhang, P.; Qi, Q.; Deng, H. Transient Vibration Response Analysis of Underwater Cylindrical Shells Based on Precise Integration Method. *Ocean Eng.* **2026**, *358*, 125881. [CrossRef]
17. Chu, S.; Featherston, C.; Kim, H.A. Design of Stiffened Panels for Stress and Buckling via Topology Optimization. *Struct. Multidiscip. Optim.* **2021**, *64*, 3123–3146. [CrossRef]
18. Putra, G.L.; Kitamura, M.; Takezawa, A. Structural Optimization of Stiffener Layout for Stiffened Plate Using Hybrid GA. *Int. J. Nav. Archit. Ocean Eng.* **2019**, *11*, 809–818. [CrossRef]
19. Liu, C.; Ahn, C.R.; An, X.; Lee, S. Life-Cycle Assessment of Concrete Dam Construction: Comparison of Environmental Impact of Rock-Filled and Conventional Concrete. *J. Constr. Eng. Manag.* **2013**, *139*, A4013009. [CrossRef]
20. Mostafaei, H.; Keshavarz, Z.; Rostampour, M.A.; Mostofinejad, D.; Wu, C. Sustainability Evaluation of a Concrete Gravity Dam: Life Cycle Assessment, Carbon Footprint Analysis, and Life Cycle Costing. *Structures* **2023**, *53*, 279–295. [CrossRef]
21. U.S. Environmental Protection Agency. Environmental Fluid Dynamics Code (EFDC). Available online: https://www.epa.gov/hydrowq/environmental-fluid-dynamics-code-efdc (accessed on 13 July 2026).
22. Hamrick, J.M. *A Three-Dimensional Environmental Fluid Dynamics Computer Code: Theoretical and Computational Aspects*; Special Report No. 317 of Applied Marine Science and Ocean Engineering; Virginia Institute of Marine Science, College of William and Mary: Gloucester Point, VA, USA, 1992; Volume 63. [CrossRef]
23. Çengel, Y.A.; Cimbala, J.M. *Fluid Mechanics: Fundamentals and Applications*, 4th ed.; SI Units; McGraw-Hill: Singapore, 2020.
24. Thang, N.D. Gate Vibrations Due to Unstable Flow Separation. *J. Hydraul. Eng.* **1990**, *116*, 342–361. [CrossRef]
25. Kampel, I.; Prenner, R.; Krouzecky, N. Pressure Fluctuations on Underflow Gates of Weirs Due to Upstream Vortex Generation. *Mater. Today Proc.* **2017**, *4*, 5833–5838. [CrossRef]
26. Budynas, R.G.; Nisbett, J.K.; Shigley, J.E. *Shigley's Mechanical Engineering Design*, 11th ed.; SI Units; McGraw-Hill: New York, NY, USA, 2021.
27. Fédération Internationale du Béton (FIB). *Design of Anchorages in Concrete*; FIB Bulletin No. 58; International Federation for Structural Concrete: Lausanne, Switzerland, 2011; ISBN 978-2-88394-098-7.
28. *EN 1992-4*; Eurocode 2—Design of Concrete Structures—Part 4: Design of Fastenings for Use in Concrete. European Committee for Standardization: Brussels, Belgium, 2018.

29. Cho, S.S.H.; Chan, S.L. *Guide on Design of Post-Installed Anchor Bolt Systems in Hong Kong*; Hong Kong Institute of Steel Construction: Hong Kong, 2016.
30. Hibbeler, R.C. *Mechanics of Materials*, 11th ed.; Pearson: Hoboken, NJ, USA, 2022.
31. *EN 10088-2:2024*; Stainless Steels—Part 2: Technical Delivery Conditions for Sheet/Plate and Strip of Corrosion-Resisting Steels for General Purposes. European Committee for Standardization: Brussels, Belgium, 2024.
32. Hibbeler, R.C. *Engineering Mechanics: Statics*, 15th ed.; Pearson: Hoboken, NJ, USA, 2022.
33. Choi, J.W.; Joo, H.J.; Kim, J.M.; Lee, K.S.; Yoon, S.J. An Analytical Study on the Structural Performance Evaluation of the Multistage Overturing Movable Gate. *J. Korean Soc. Steel Constr.* **2013**, *25*, 613–622. [CrossRef]
34. Alinia, M.M.; Shirazi, R.S. On the Design of Stiffeners in Steel Plate Shear Walls. *J. Constr. Steel Res.* **2009**, *65*, 2069–2077. [CrossRef]
35. Xiao, J.-L.; Liu, J.; Liu, Y.-F.; Fan, J.-S. Inelastic Numerical Analysis-Based Optimal Design of Longitudinal Stiffeners in Steel Web Plates. *J. Constr. Steel Res.* **2026**, *238*, 110201. [CrossRef]
36. Al-Yacouby, A.M.; Mazli, A.A.; Liew, M.S.; Ratnayake, R.M.C.; Samarakoon, S.M.K. Finite Element Analysis of Steel Plates with Rectangular Openings Subjected to Axial Stress. *Materials* **2022**, *15*, 4421. [CrossRef]
37. Antipov, Y.A. Nonlinear Bending Models for Beams and Plates. *Proc. R. Soc. A Math. Phys. Eng. Sci.* **2014**, *470*, 20140064. [CrossRef]
38. *ASTM A572/A572M-21*; Standard Specification for High-Strength Low-Alloy Columbium-Vanadium Structural Steel. ASTM International: Conshohocken, PA, USA, 2021.
39. Moynihan, M.C.; Allwood, J.M. Utilization of Structural Steel in Buildings. *Proc. R. Soc. A Math. Phys. Eng. Sci.* **2014**, *470*, 20140170. [CrossRef]
40. Sen, P.; Yang, J.-B. Multiple-Criteria Decision-Making in Design Selection and Synthesis. *J. Eng. Des.* **1995**, *6*, 207–230. [CrossRef]
41. Hariyadi; Munemoto, S.; Sonoda, Y. Experimental Analysis of Anchor Bolt in Concrete under the Pull-Out Loading. *Procedia Eng.* **2017**, *171*, 926–933. [CrossRef]
42. Yu, Q.M.; Yang, X.J.; Zhou, H.L. An Experimental Study on the Relationship between Torque and Preload of Threaded Connections. *Adv. Mech. Eng.* **2018**, *10*, 1687814018797033. [CrossRef]
43. Naruse, T.; Shibutani, Y. Nonlinear Bending Stiffness of Plates Clamped by Bolted Joints under Bending Moment. *J. Solid Mech. Mater. Eng.* **2012**, *6*, 832–843. [CrossRef]
44. Cheraghi-Shirazi, N.; Kabiri-Samani, A.R.; Boroomand, B. Numerical Analysis of Rubber Dams Using Fluid–Structure Interactions. *Flow Meas. Instrum.* **2014**, *40*, 91–98. [CrossRef]
45. Watson, L.T.; Suherman, S.; Plaut, R.H. Two-Dimensional Elastica Analysis of Equilibrium Shapes of Single-Anchor Inflatable Dams. *Int. J. Solids Struct.* **1999**, *36*, 1383–1398. [CrossRef]
46. Guo, W.; Zeng, W.; Gao, X.; Ren, Y. Analysis of Air-Inflated Rubber Dam for Flood-Fighting at the Subway Entrance. *J. Flood Risk Manag.* **2023**, *16*, e12872. [CrossRef]
47. Kean, J.W.; Kuhnle, R.A.; Smith, J.D.; Alonso, C.V.; Langendoen, E.J. Test of a Method to Calculate Near-Bank Velocity and Boundary Shear Stress. *J. Hydraul. Eng.* **2009**, *135*, 588–601. [CrossRef]
48. Farhoudi, J.; Shayan, H.K. Investigation on Local Scour Downstream of Adverse Stilling Basins. *Ain Shams Eng. J.* **2014**, *5*, 361–375. [CrossRef]
49. Mahmoudi, B.; Hemmati, M.; Yasi, M.; Ahmad Hamidi, S. Experimental Study of the Time Scale for Local Scour Downstream of Parallel Sluice Gates. *J. Irrig. Drain. Eng.* **2023**, *149*, 06023004. [CrossRef]
50. Cheng, B.; Wang, J.; Shi, P. Improving the Compression Behaviors of Perforated Plates with Slotted Holes Using Strengthening Stiffeners. *J. Struct. Eng.* **2015**, *141*, 04015048. [CrossRef]
51. Haffar, M.Z.; Ádány, S. On the Buckling of Longitudinally Stiffened Plates, Part 1: Modal Analysis by the Constrained Finite Element Method. *Thin-Walled Struct.* **2019**, *145*, 106394. [CrossRef]
52. Choi, B.H.; Andico, A.N.P.; Choi, S.H. Local Buckling of Longitudinally Stiffened Plates with Rotational Stiffness of Closed-Section Ribs. *J. Constr. Steel Res.* **2020**, *167*, 105876. [CrossRef]
53. Fang, D.; Kenny, P.; Mueller, C. Material Efficiency as a Key Opportunity to Reduce Embodied Carbon in Structural Systems: Data Insights from 226 Fully Designed Projects. *J. Struct. Eng.* **2026**, *152*, 04025275. [CrossRef]
54. Zhang, S.; Pang, B.; Zhang, Z. Carbon Footprint Analysis of Two Different Types of Hydropower Schemes: Comparing Earth-Rockfill Dams and Concrete Gravity Dams Using Hybrid Life Cycle Assessment. *J. Clean. Prod.* **2015**, *103*, 854–862. [CrossRef]

Disclaimer/Publisher's Note: The statements, opinions and data contained in all publications are solely those of the individual author(s) and contributor(s) and not of MDPI and/or the editor(s). MDPI and/or the editor(s) disclaim responsibility for any injury to people or property resulting from any ideas, methods, instructions or products referred to in the content.